Phase transition and Superconductivity in ReS2, ReSe2 and ReTe2

Journal:	*Physical Chemistry Chemical Physics*
Manuscript ID	CP-ART-08-2018-005333.R2
Article Type:	Paper
Date Submitted by the Author:	03-Nov-2018
Complete List of Authors:	zhang, Jurong; Jilin University, College of Physics; Sun, Ermiao; Jilin University Feng, Xiaolei; University of Cambridge Liu, Hanyu; Jilin University, State Key Laboratory of Superhard Materials Redfern, Simon; University of Cambridge, Department of Earth Sciences Kanchana, V; Indian Institute of Technology Hyderabad, Department of Physics Liu, Guangtao; Jilin University, State Key Laboratory of Superhard Materials ChangChun Wang, Hongbo; State Key Lab of Superhard Materials, Jilin University

Phase transition and Superconductivity in ReS_2, $ReSe_2$ and $ReTe_2$

Jurong Zhang[1], Ermiao Sun[1], Xiaolei Feng[1, 2], Hanyu Liu[3,1], Simon A. T. Redfern[2], V. Kanchana[4],Guangtao Liu[1*], Hongbo Wang[1*]

[1]*State Key Laboratory of Superhard Materials, College of Physics, Jilin University, Changchun 130012, China*

[2]*Department of Earth Sciences, University of Cambridge, Downing Street, Cambridge CB2 3EQ, UK*

[3]*Innovation Center for Computational Physics Method and Software, College of Physics, Jilin University, Changchun 130012, China*

[4]*Department of Physics, Indian Institute of Technology Hyderabad, Kandi, Medak 502 285, Telengana, India*

*Corresponding author: 07455@163.com;whb2477@jlu.edu.cn

Abstract

Transition metal dichalcogenides have attracted significant attention, due to both fundamental interest as well as their potential applications. Here, we have systematically explored the crystal structures of ReX_2 (X= S, Se, Te) over the pressure range 0–300 GPa, employing swarm-intelligence-based structure prediction methodology. Several new structures are found to be stable at high pressures. The calculated enthalpy of formation suggested that all predicted high-pressure structures are stable against decomposition into elemental end-members. Moreover, we found the simulated X-ray diffraction patterns of $ReSe_2$ are in good agreement with experimental data. Pressure-induced metallization of ReX_2 has been revealed from the analysis of electronic structure. Our electron-phonon coupling calculations indicate $ReSe_2$ and $ReTe_2$ are superconducting phases at high pressures.

Introduction

Transition-metal dichalcogenides (TMX_2) (TM=W, Mo, Re, Rb, Tc etc.; X = S,

Se, Te) are mostly layered materials, in which TM atomic layers are sandwiched between two chalcogen atom layers, forming an X-M-X sandwiched structure[1-5]. The X-M-X trilayers then stack together via weak van der Waals (vdW) interactions, resulting in different phases of transition-metal dichalcogenides (TMDs) such as 1T, 1T′, $2H_c$, 2Ha and 3R[4,6]. Therefore, the bulk phases of TMDs exhibit a broad spectrum of electronic behaviors ranging from insulators to metals or even superconductors[4,6,7].

ReX_2 (X=S, Se, Te) has attracted significant recent attention, with reports of photoluminescent properties, catalytic behavior and promising solar-cell applications[8-11]. ReX_2 compounds are semiconducting layered transition metal dichalcogenides that exhibit a low-symmetry stable distorted 3R CdCl structure (*P*-1) at ambient conditions[12-14], in which Re atoms are surrounded by six chalcogen atoms in trigonal prism coordination at ambient conditions. The effects of pressure in reducing inter-atomic distances and modifying crystal structures are well known, thus pressure may provide a route to engineer and improve the physical and chemical properties of materials[15]. An early experimental study on ReS_2 revealed a high-pressure phase at ~11.3 GPa[16]. Recently, Zhou *et al.*[17] reported that the distorted-3R (*P*-1) phase, stable at 0 GPa, will transform to a distorted-1T phase, also with *P*-1 symmetry, at 3 GPa, and then to a non-layered $I4_1/amd$ structure at 90 GPa, which is stable up to at least 200 GPa. Remarkably, the nonlayered $I4_1/amd$ structure of ReS_2 shows superconductivity (with $T_c \approx 2$ K) below 100 GPa. The selenide equivalent, $ReSe_2$, was found to undergo a phase transition at ~10 GPa using angular-dispersive x-ray diffraction (ADXRD)[18] with a new peak appearing, however, the crystal structure and properties of $ReSe_2$ of the new phase have not been defined. A similar phase transition in $ReSe_2$ was also found at ~7 GPa by Naumov, as confirmed by Raman spectroscopy which showed the redistribution of Raman peak intensities and a discontinuity in the pressure dependence of the vibration frequencies at this pressure[19]. The two experimental works on $ReSe_2$ therefore support each other. For the telluride, $ReTe_2$, the high-pressure behavior is still completely unknown.

In this work, we have explored the high-pressure behaviors of ReX_2 over the pressure range 0–300 GPa. By using the particle swarm optimization technique[20], in

combination with ab initio calculations, we have discovered a number of proposed high-pressure candidate structures and analyzed their electronic properties, which reveal pressure-induced metallization in this family of solids.

Computational details

We have studied the structures of ReX_2 using the particle swarm optimization technique implemented in the CALYPSO code[20,21]. This has been proved to be a reliable method for the successful predictions of high pressure structures for a wide variety of systems[22,23]. We research the structures of ReX_2 (X=S, Se, Te) system with unit cell sizes ranging from 1 to 4 formulas per simulation cell at 0, 50, 100, 150, 200, 250, 300 GPa. Each generation contained 30 structures, and the first generation was produced randomly with symmetry constraint. The 60% lowest-enthalpy structures of each generation were used to produce the structures in the next generation by local Particle Swarm Optimization (PSO) technique, and the remaining 40% structures were randomly generated within symmetry constraint to enhance the structural diversity. Total-energy calculations and geometrical optimization for these structures were performed in the framework of density functional theory within the Perdew-Burke-Ernzerhof[24] parametrization of generalized gradient approximation[25] as implemented in the VASP code[26]. In order to obtain accurate results, the vdW interaction was taken into consideration. The interaction among electrons and ions was simulated by the all-electron projector augmented-wave (PAW) method[27] and the $5s^25p^66s^25d^5$, $3s^23p^4$, $4s^24p^4$, $5s^25p^4$ electrons were set as valence electrons for the Re, S, Se and Te atoms, respectively. We chose a cutoff energy of 500 eV as the plane-wave kinetic energy cutoff and used Monkhorst-Pack[28] k meshes with grid spacing of $2\pi \times 0.03$ $Å^{-1}$. The dynamical stability of crystal structures was calculated using finite displacement as implemented in the PHONOPY code[29]. Superconducting properties were calculated within the framework of linear response theory through the Quantum-ESRESSO code[30]. The plane-wave pseudopotential method of the ultrasoft vanderbilt pseudopotentials within density functional perturbation theory were used to calculate the EPC (electron-phonon coupling). We choose 50 Ry for the kinetic energy cutoff of the plane-wave

basis after testing for convergence. The *k*-space and *q*-point integrations over the Brilloiun zone (BZ) were performed on a 28×28×6 grid and a 14×14×3 grid of the $P6_3/mmc$ phase of $ReSe_2$, a 20×20×6 grid and 10×10×3 grid of the $I4/mmm$ phase of $ReSe_2$ and a 24×24×6 grid and 12×12×3 grid of the $I4/mmm$ phase of $ReTe_2$, respectively. The crystal-orbital Hamilton population was calculated using the LOBSTER code[31] for the binding analysis of ReX_2 (X=S, Se, Te). The EPC spectral function is expressed by the phonon linewidth $\gamma_{\vec{q}j}$ arising from electron-phonon scattering[32-34],

$$\alpha^2F(\omega)=\frac{1}{2\pi N_f}\sum_{\vec{q}j}\frac{\gamma_{\vec{q}j}}{\omega_{\vec{q}j}}\delta(\hbar\omega-\hbar\omega_{\vec{q}j})w(\vec{q}) \qquad 1.1$$

where N_f is the electronic density of states/atom and spin at the Fermi level. The linewidth of a phonon mode j at wave vector $\vec{q}$, $\gamma_{\vec{q}j}$, resulting from electron-phonon interaction is as follows:

$$\gamma_{\vec{q}j}=2\pi\omega_{\vec{q}j}\sum_{nm}\int\frac{d^3\vec{k}}{\Omega_{BZ}}\left|g^j_{kn,k+\vec{q}m}\right|^2\delta(\varepsilon_{\vec{k}n}-\varepsilon_F)\delta(\varepsilon_{\vec{k}+\vec{q}m}-\varepsilon_F), \qquad 1.2$$

where the sum is over the first BZ, with Ω_{BZ} as the volume of the BZ, $\varepsilon_{\vec{k}n}$ is the energy of bands measured relative to the Fermi level at point $\vec{k}$, and $g^j_{kn,\vec{k}+\vec{q}m}$ represent the electron-phonon matrix element. The EPC parameter λ can be expressed as:

$$\lambda=2\int_0^\infty\frac{\alpha^2F(\omega)}{\omega}d\omega\approx\sum_{\vec{q}j}\lambda_{\vec{q}j}w(\vec{q}), \qquad 1.3$$

where $w(\vec{q})$ is the weight of a $\vec{q}$ point in the first BZ. Finally, the superconducting transition temperature T_c can be estimated by the Allen-Dynes modified McMillan

equation[35] as

$$T_C = \frac{\omega_{\log}}{1.2}\exp\left[-\frac{1.04(1+\lambda)}{\lambda-\mu^*(1+0.62\lambda)}\right], \quad 1.4$$

where $\omega_{\log}$ is the logarithmic average frequency, and μ^* is the Coulomb pseudopotential.

Results and discussions

At ambient pressure, the experimentally-observed distorted-3R[13,14] phase (space group *P*-1) was accurately shown to be stable by our calculations. The interesting thing is that at high pressure, the *P*-1 phase transform to the *R*-3*m* phase after optimization as shown by dashed line in Fig. 1, which is also a layer phase. The enthalpy curves of candidate structures of ReX_2 relative to $P6_3/mmc$ are presented as a function of pressure in Fig. 1. All of the structural relaxations are based on the optB86b function together with the vdW-DF correction[36], which minimize the errors compared to the calculation using GGA-PBE as shown in Table 1. A succession of phase transitions from *P*-1 (distorted-3R)→*P*-1′(distorted-1T′)→$P6_3/mmc$ ($2H_c$) →$I4_1/amd$→$I4/mmm'$ of ReS_2 was clearly revealed at 3.0 GPa, 96.5 GPa, 99.5 GPa and 248.2 GPa respectively. The *P*-1′ phase and $I4_1/amd$ phase in this work are consistent with earlier reports in Zhou et al.'s work[17]. Two new structures, $P6_3/mmc$ and $I4/mmm'$, were found to be most stable in the pressure range of 96.5–99.5 GPa and > 248.2 GPa, respectively. $ReSe_2$ also show a complex sequence of phase transitions from *P*-1 (distorted-3R) →*P*-1′ (distorted-1T′) →$P6_3/mmc$ ($2H_c$)→$I4/mmm$→$I4/mmm'$ at 21.9 GPa, 69.2 GPa, 106 GPa and 231.7 GPa respectively. Fig. 2 shows a comparison of the experimental XRD[18] patterns for $ReSe_2$ and the simulated XRD patterns of the ambient-pressure structure and the *P*-1′ phase predicted for 10.5 GPa. It can be seen that the peak marked with a star is a "fingerprint" of the new phase[18], and the next three peaks in the experimental data are in good agreement with the XRD of *P*-1′ in our work as well. The strongest peak in the figure is from the *P*-1 phase for the sample was dominated by *P*-1 phase[18]. Therefore, our result demonstrates that the phase found by Kao et al. is indeed a distorted 1T' phase with *P*-1 space group. In contrast to ReS_2 and $ReSe_2$, in $ReTe_2$, the ground state

of the distorted-3R (*P*-1) structure directly transforms to a *I*4/*mmm* phase at 50 GPa, which remains the lowest-enthalpy structure of $ReTe_2$ up to 300 GPa. All the high-pressure structures are stable against decomposition into elemental end-members as shown by the thermodynamic calculations (Fig. 1). The first order phase transitions are indicated by the density increases across each transition, which are ~3% , ~1.9%, ~2.5% for ReS_2, ~15.2%, ~8.3% and ~1.3% for $ReSe_2$, and 4.7 % for $ReTe_2$, respectively.

The high-pressure phases and corresponding unit cells of ReX_2 (X=S, Se, Te) are depicted in Fig. 3 and the detailed structure information is shown in table 3. The *P*-1′ phase (Fig 3 (a, f)) is a distorted-1T layer structure formed by a shear of the ground state distorted-3R structure. Within each layer, the Re atom is six-fold coordinated by X to form a ReX_6 octahedron. The $P6_3/mmc$ phase of ReX_2 (X=S, Se) corresponds to a ReX_6 triangular prism layer structure (Fig 3 (b, g)), which is a universal ground state in TMX_2 compounds. The $I4_1/amd$ phase (Fig 3 (c, h)) of ReS_2 was previously proposed by Zhou et al.[17] and is a close-stacking structure formed by ReS_6 edge-sharing irregular octahedra. The *I*4/*mmm* structure (Fig 3 (d, i)) is composed of face-sharing ReX_8 cuboid layers, with adjacent layers displaced *a*/2 and *b*/2 along the *x* and *y* axes, respectively. The *I*4/*mmm*′ structure (Fig 3 (e, j)) consists of layers of close-packed Re_3X_{18} units which can be considered as the stacking of three face-sharing ReX_8 cubes bonded via two X atoms along the *z* axis. The adjacent layers are displaced *a*/2 and *b*/2 with respect to each other along the *x* and *y* axes. As expected from general pressure-coordination trends[37], the coordination number of Re atom changes from 6 (*P*-1′, $P6_3/mmc$, $I4_1/amd$) to 8 (*I*4/*mmm*, *I*4/*mmm*′), and the coordination number of X by X atom increases from 2 (*P*-1) to 3 (*P*-1′, $P6_3/mmc$, $I4_1/amd$), and finally to 4 (*I*4/*mmm*, *I*4/*mmm*′). With increasing of pressure, the Re-X distance is almost unchanged, but the X-X distance decreases significantly and becomes more comparable to the X-Re distance. This suggests that the X-X coordination environment might play an important role in determining the transition sequence. Indeed, it is found that the three phases with X-X coordination number of 3 (*P*-1′, $P6_3/mmc$, $I4_1/amd$) do not appear in the sequence of $ReTe_2$ and $I4_1/amd$ does not present in $ReSe_2$. It seems that the X-X coordination number of 3 becomes more unfavorable with increasing of both the atomic radii of X

and pressure.

In order to further explore and verify the structural stability of these structures, the phonon density of states (PHDOS) of all high-pressure phases of ReX_2 (X=S, Se, Te) were calculated using the supercell method (Fig.4). No imaginary phonon frequencies are found across the whole Brillouin zone, demonstrating the dynamical stability of these structures. Because pressure induces an increase in the force constants between atoms, the phonons of ReX_2 move to higher frequency with increasing pressure.

The electronic band structure of *P*-1′of ReS_2 at 60 GPa reveals its semi-conductor characteristics (Fig. 5). With increasing pressure to 80 GPa, however, the bands already cross through the Fermi level and the material acts as a semimetal, with weak metallic properties. Our observations are in line with Zhou's work, which also found metallization in this phase at 70 GPa[17]. Similar metallization is also observed in the *P*-1′ phase of $ReSe_2$, which is a semiconductor at 40 GPa and a semimetal at 60 GPa. Naumov et al.[19] also described the metallization of $ReSe_2$, from resistivity curve analysis. For $ReTe_2$, the ground state of the *P*-1 phase becomes metallic below 10 GPa according to the bands shown in Fig. 5(e, f). It can be seen, therefore, that pressure induces metallization of ReX_2 (X=S, Se, Te). For all the semimetal states of ReX_2 (X=S, Se, Te), there are two bands through the Feri level: one is an electron-like band, while the other is a hole-like band.

According to the projected electronic density of states (PDOS), the *P*-1′ phase of ReS_2 and $ReSe_2$ are poor metals. As expected, the total DOS at the Fermi level mainly comprises contributions from the orbitals of Re 5d, S 3p, Se 4p, and Te 5p. There are obvious hybridization in *P*-1′ and $P6_3/mmc$ phases of $ReSe_2$(Fig. 6). Superconducting behavior has been extensively studied in transition metal dichalcogenides such as WTe_2, TaS_2, $NbSe_2$, MoS_2, ReS_2, among others[4,6,17,38,39]. From the band and DOS information, ReX_2 (X=S, Se, Te) is metallic at high pressure. In addition, however, we have further studied the superconductivity of $ReSe_2$ and $ReTe_2$ below 200 GPa. We note that superconductivity in ReS_2 was reported previously by Zhou et al.[17], therefore we have not repeated those calculations. The Eliashberg phonon spectral function $\alpha^2F(\omega)$, logarithmic average phonon frequency ω_{log}, and the electron-phonon coupling

parameter λ, of the $P6_3/mmc$ structure of $ReSe_2$ at 100 GPa, the $I4/mmm$ structure of $ReSe_2$ at 150 GPa, and the $I4/mmm$ structure of $ReTe_2$ at 50 GPa are shown in Fig.7. The resulting values of λ are found to be 0.210, 0.238 and 0.245, respectively. The $\mu*$ is Coulomb pseudopotential parameter and it remains challenging to directly derive an accurate $\mu*$ from first-principles theory but an upper bound on $\mu*$ is estimated to be 0.25[32]. In the revision, we recalculated the superconducting transition temperatures (Tc) with a typical Coulomb pseudopotential parameter[40] $\mu^* = 0.13$, and the Tc of the $P6_3/mmc$ structure of $ReSe_2$ at 100 GPa, the $I4/mmm$ structure of $ReSe_2$ at 150 GPa, and the $I4/mmm$ structure of $ReTe_2$ at 50 GPa are 1.0 K, 2.0 K and 1.4 K, respectively. From the PHDOS, Eliashberg EPC spectral function $\alpha^2F(\omega)$ and the electron-phonon integral $\lambda(\omega)$ (Fig .7), it is evident that for the $P6_3/mmc$ phase of $ReSe_2$, the low-frequency translational vibrations from Se and Re atoms contribute similarly to λ and the high-frequency translational vibrations from Se make more contribution than high-frequency translational vibrations from the Re to λ and the same tendency was also found in $I4/mmm$ phase of $ReSe_2$. In $I4/mmm$ phase of $ReTe_2$, Te atoms vibrations make more contribution than Re atoms vibrations to the overall EPC constant. We have added these analysis in the revision.

We have used crystal orbital Hamilton population (COHP) analysis to determine the strength and nature of the chemical bonding of Re-X (X=S, Se, Te) pairs in all high-pressure phases. The averaged COHP of Re-X (X=S, Se, Te) atom pairs are shown in Fig. 8. The negative value (low energy region) of the COHP indicates any bonding character between such Re-X (X=S, Se, Te) pairs. The integrated crystal orbital Hamilton population (ICOHP) was calculated to analyze the strength and nature of chemical bonding between Re atoms and X (S, Se, Te) atoms, as shown in Table 2. For ReS_2, the Re-S bonds in the $P6_3/mmc$ structure (-3.48) are stronger than the Re-S bonds in the $I4/mmm'$ structure (-2.74) but similar to those in the $I4_1/amd$ (-3.74) phase. The ICOHP value of Re-Se bonds of the $P\text{-}1'$(-3.54) and $P6_3/mmc$ (-3.33) phases of $ReSe_2$ are also similar, however they are all smaller than the ICOHP of $I4/mmm$ (-2.97) and $I4/mmm'$(-2.08) $ReSe_2$, indicating that the Re-Se bonds in the $P\text{-}1'$ and $P6_3/mmc$ phases are stronger than those in the $I4/mmm'$ phase of $ReSe_2$. Similarly, the Re-Te bonds of

six-fold coordinated Re in *P*-1′ $ReTe_2$ are stronger than the Re-Te bonds in the *I*4/*mmm* phase, as revealed by the ICOHP of *P*-1 (-3.12) $ReTe_2$ being larger than that of the *I*4/*mmm* (-2.22) phase.

Conclusions

In summary, we have investigated high-pressure behavior of the transition metal dichalcogenide ReX_2 system. Five high-pressure phases, *P*-1′, $P6_3/mmc$, $I4_1/amd$, *I*4/*mmm* and *I*4/*mmm*′, were predicted in the ReX_2 family of compounds and are found to be energetically stable over certain pressure ranges. Thermodynamical calculations revealed that all the high-pressure phase of ReX_2 are stable with respect to elemental decomposition up at least up to 300 GPa. With increasing pressure, the coordinated environment changes from ReX_6 octahedra or trigonal prisms to ReX_8 cuboids. Moreover, our electron-phonon coupling calculations have revealed the superconducting potential of metallic ReX_2 phases. Our simulated X-ray diffraction patterns, from our computed structures for $ReSe_2$, are in good agreement with previous experimental data.

Notes

The authors declare no competing financial interest.

Acknowledgement

This work was supported by NSAF No. U1530124; National Natural Science Foundation of China under Grants No. 11474128, No. 11774127, No. 11534003 and No. 11764043; the National Key Research and Development Program of China under Grant No. 2016YFB0201200, No. 2016YFB0201201, and No. 2017YFB0701503; the 2012 Changjiang Scholars Program of China supported by Program for JLU Science and Technology Innovative Research Team; the Science Challenge Project No. TZ2016001 and the NSF-CREST Center for Innovation, Research and Education in Environmental Nanotechnology with Grant Number HRD-1736093 and NASA with Grant 17-EPSCoRProp-0032.

References

1 Marezio, M.; Dernier, P.; Menth, A.; Hull Jr, G. *J. Solid State Chem.* 1972**, 4**, 425-429.

2 Fang, C.; Wiegers, G.; Haas, C.; De Groot, R. *J. Phys.: Condens. Matter* 1997**, 9**, 4411.

3 Chhowalla, M.; Shin, H. S.; Eda, G.; Li, L.-J.; Loh, K. P.; Zhang, H. *Nat. Chem.* 2013, **5**, 263.

4 Lu, P.; Kim, J.-S.; Yang, J.; Gao, H.; Wu, J.; Shao, D.; Li, B.; Zhou, D.; Sun, J.; Akinwande, D. *Phys. Rev. B* 2016**, 94**, 224512.

5 Brown, B. E. *Acta Crystallogr.* 1966, **20**, 268-274.

6 Kohulák, O.; Martoňák, R. *Phys. Rev. B* 2017, **95**, 054105.

7 Wang, X.; Chen, X.; Zhou, Y.; Park, C.; An, C.; Zhou, Y.; Zhang, R.; Gu, C.; Yang, W.; Yang, Z. *Sci. Rep.* 2017, **7**, 46694.

8 Broadbent, H. S.; Slaugh, L. H.; Jarvis, N. L. *J. Am. Chem. Soc.* 1954, **76**, 1519-1523.

9 Wheeler, B. L.; Leland, J. K.; Bard, A. J. *J. Electrochem. Soc* 1986, **133**, 358-361.

10 Koffyberg, F.-P.; Dwight, K.; Wold, A. *Solid State Commun.* 1979, **30**, 433-437.

11 Lin, Y.-C.; Komsa, H.-P.; Yeh, C.-H.; Bjorkman, T.; Liang, Z.-Y.; Ho, C.-H.; Huang, Y.-S.; Chiu, P.-W.; Krasheninnikov, A. V.; Suenaga, K. *ACS nano* 2015**, 9**, 11249-11257.

12 Jariwala, B.; Thamizhavel, A.; Bhattacharya, A. *J. Phys. D: Appl. Phys.* 2016, **50**, 044001.

13 Larchev, V.; Popova, S. *Inorg. Mater.* 1976, **12**, 1130-1132.

14 Lamfers, H.-J.; Meetsma, A.; Wiegers, G.; De Boer, J. *J. Alloys Compd.* 1996, **241**, 34-39.

15 Zhang, L.; Wang, Y.; Lv, J.; Ma, Y. *Nat. Rev. Mater.* 2017, **2**, 17005.

16 Hou, D.; Ma, Y.; Du, J.; Yan, J.; Ji, C.; Zhu, H. *J. Phys. Chem. Solids* 2010, **71**, 1571-1575.

17 Zhou, D.; Zhou, Y.; Pu, C.; Chen, X.; Lu, P.; Wang, X.; An, C.; Zhou, Y.; Miao,

F.; Ho, C.-H. *npj Quantum Materials* 2017, **2**, 19.

18 Kao, Y.-C.; Huang, T.; Lin, D.-Y.; Huang, Y.-S.; Tiong, K.-K.; Lee, H.-Y.; Lin, J.-M.; Sheu, H.-S.; Lin, C.-M. *J. Chem. Phys.* 2012, **137**, 024509.

19 Naumov, P.; ElGhazali, M.; Mirhosseini, H.; Süß, V.; Morosan, E.; Felser, C.; Medvedev, S. *J. Phys.: Condens. Matter* 2017, **30**, 035401.

20 Wang, Y.; Lv, J.; Zhu, L.; Ma, Y. *Phys. Rev. B* 2010, **82**, 094116.

21 Wang, Y.; Lv, J.; Zhu, L.; Ma, Y. *Comput. Phys. Commun.* 2012, **183**, 2063-2070.(

22 Wang, H.; John, S. T.; Tanaka, K.; Iitaka, T.; Ma, Y. *Proc. Natl. Acad. Sci. U.S.A.* 2012, **109**, 6463-6466.

23 Liu, H.; Naumov, I. I.; Hoffmann, R.; Ashcroft, N.; Hemley, R. J. *Proc. Natl. Acad. Sci. U.S.A.* 2017, **114**, 6990-6995.

24 Perdew, J. P.; Chevary, J. A.; Vosko, S. H.; Jackson, K. A.; Pederson, M. R.; Singh, D. J.; Fiolhais, C. *Phys. Rev. B* 1992, **46**, 6671.

25 Perdew, J. P.; Burke, K.; Ernzerhof, M. *Phys. Rev. Lett.* 1996, **77**, 3865.

26 Kresse, G.; Furthmüller, J. *Phys. Rev. B* 1996, **54**, 11169.

27 Blöchl, P. E. *Phys. Rev. B* 1994, **50**, 17953.

28 Monkhorst, H. J.; Pack, J. D. *Phys. Rev. B* 1976, **13**, 5188.

29 Togo, A.; Oba, F.; Tanaka, I. *Phys. Rev. B* 2008, **78**, 134106.

30 Giannozzi, P.; Baroni, S.; Bonini, N.; Calandra, M.; Car, R.; Cavazzoni, C.; Ceresoli, D.; Chiarotti, G. L.; Cococcioni, M.; Dabo, I. *J. Phys.: Condens. Matter* 2009, **21**, 395502.

31 Maintz, S.; Deringer, V. L.; Tchougréeff, A. L.; Dronskowski, R. *Chem.* 2016, **37**, 1030-1035.

32 Allen, P. B.; Silberglitt, R. *Phys. Rev. B* 1974, **9**, 4733.

33 Allen, P. B. *Phys. Rev. B* 1972, **6**, 2577.

34 Bardeen, J.; Cooper, L. N.; Schrieffer, J. R. *Phys. Rev.* 1957, **108**, 1175.

35 Allen, P. B.; Dynes, R. *Phys. Rev. B* 1975, **12**, 905.

36 Dion, M.; Rydberg, H.; Schröder, E.; Langreth, D. C.; Lundqvist, B. I. *Phys. Rev. Lett.* 2004, **92**, 246401.

37 Gao, G.; Hoffmann, R.; Ashcroft, N. W.; Liu, H.; Bergara, A.; Ma, Y. *Phys. Rev.*

B 2013, **88**, 184104.

38 Boaknin, E.; Tanatar, M.; Paglione, J.; Hawthorn, D.; Ronning, F.; Hill, R.; Sutherland, M.; Taillefer, L.; Sonier, J.; Hayden, S. *Phys. Rev. Lett.* 2003, **90**, 117003.

39 Sipos, B.; Kusmartseva, A. F.; Akrap, A.; Berger, H.; Forró, L.; Tutiš, E. *Nat. Mater.* 2008, **7**, 960.

40 Peng, F.; Sun, Y.; Pickard, C. J.; Needs, R. J.; Wu, Q.; Ma, Y. Phys. Rev. Lett. 2017, **119** (10), 107001.

Figure Caption:

Fig. 1. The enthalpies (relative to the *P*6$_3$/*mmc* structure) as a function of pressure of ReS_2 (a), $ReSe_2$ (b), $ReTe_2$ (c). We adopt the hP2 structure of Re; the hP3 (Se-I) phase, Se-III phase, *β*-Po phase, and bcc phase, and the fcc phase of Se; Te-I, *β*-Po phase, the bcc phase, the fcc phase of Te; oF128 phase, hP9 phase, S-II phase and the *β*-Po phase of S as the reference phases in their own stable pressure ranges.

Fig. 2. Comparison of the experimental XRD data for $ReSe_2$ with a simulated XRD pattern for the ambient-pressure structure and predicted *P*-1′ phase at 10.5 GPa. The XRD data from experiment at 10.5 GPa are shown as a black line and the simulated XRD curves of *P*-1 phase and *P*-1′ phase at 10.5 GPa are given by blue and red lines, respectively. The peak marked with an asterisk is the new peak found in experiment.

Fig. 3. The crystal structure of the *P*-1′ (a), *P*6$_3$/*mmc* (b), *I*4$_1$/*amd* (c), *I*4/*mmm*(d) and *I*4/*mmm*′ (e) phases of ReX_2 and the local coordination environment of Re (f)-(j); The gray and green balls represent Re and X (X = S, Se, Te) atoms, respectively.

Fig. 4. The atom-projected PHDOS of *P*6$_3$/*mmc* of ReS_2 at 97 GPa (a), *I*4$_1$/*amd* of ReS_2 at 100 GPa (b), *I*4/*mmm*′ of ReS_2 ta 300 GPa (c), *P*-1 of $ReTe_2$ at 0 GPa (d), *I*4/*mmm* of $ReTe_2$ at 50 GPa (e), *P*-1 of $ReSe_2$ at 0 GPa (f), *P*-1′ $ReSe_2$ at 40 GPa (g), *P*6$_3$/*mmc* of $ReSe_2$ at 100 GPa (h), *I*4/*mmm* of $ReSe_2$ at 150 GPa (i), *I*4/*mmm*′ of $ReSe_2$ at 300 GPa (j).

Fig. 5. The band structure of the *P*-1′ phase of ReS_2 at 40 GPa (a) and 80 GPa (b), the *P*-1′ phase of $ReSe_2$ at 40 GPa (c) and 60 GPa (d), and the *P*-1 phase of $ReTe_2$ at 0 GPa (e) and 10 GPa (f).

Fig. 6. The total and partial (or orbital-projected) DOS of the *P*6$_3$/*mmc* phase of ReS_2 at 97 GPa (a), the *I*4/*mmm*′ phase of ReS_2 at 300 GPa (b), the *P*-1′ phase of $ReSe_2$ at 40

GPa (c), the *P*6$_3$/*mmc* phase of $ReSe_2$ at 100 GPa (d), the *I*4/*mmm* phase of $ReSe_2$ at 150 GPa (e), the *I*4/*mmm*′ phase of $ReSe_2$ at 240 GPa and (f), the *I*4/*mmm*′ phase of $ReTe_2$ at 50 GPa (g).

Fig. 7. The calculated projected phonon density of states (lower panels), Eliashberg EPC spectral function α^2 F(ω) and its integral λ(ω) (upper panels) of (a) the *P*6$_3$/*mmc* phase of $ReSe_2$ at 100 GPa, (b) the *I*4/*mmm* phase at 150 GPa and (c) the *I*4/*mmm* phase of $ReTe_2$ at 50 GPa.

Fig. 8. The COHP of Re-S pairs for the *P*6$_3$/*mmc* structure at 97 GPa (a), *I*4$_1$/*amd* at 100 GPa (b), *I*4/*mmm*′ at 300 GPa (c); Re-Se pairs in the *P*-1′ phase at 40 GPa (d), *P*6$_3$/*mmc* at 100 GPa (e), *I*4/*mmm* 150 GPa (f), *I*4/*mmm*′ at 240 GPa(g) and Re-Te pairs in the *I*4/*mmm* phase at 50 GPa (h). The Fermi level is at the energy origin.

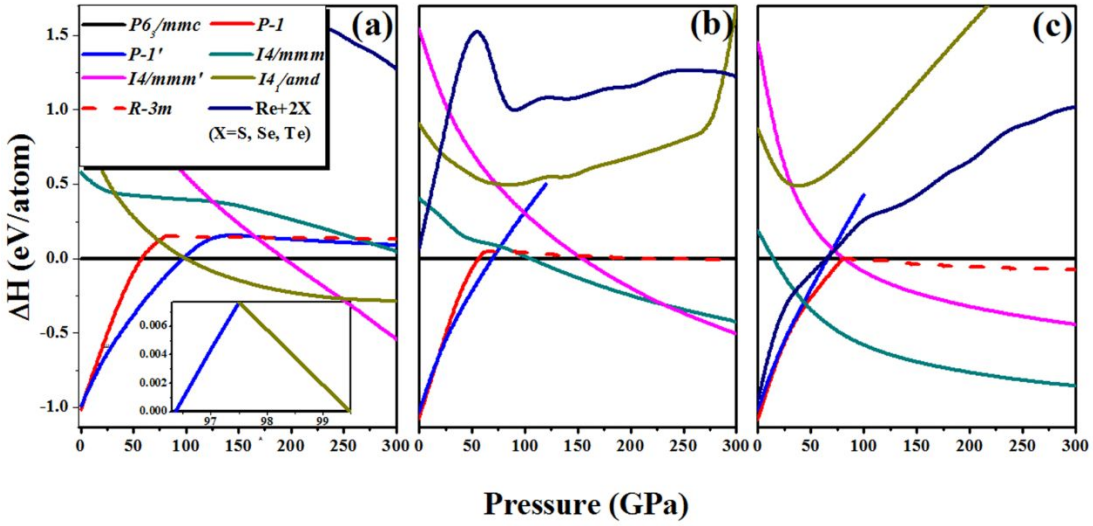
P6₃/mmc
P-1
P-1'
I4/mmm
I4/mmm'
I4₁/amd
R-3m
Re+2X
(X=S, Se, Te)
(a)
(b)
(c)
ΔH (eV/atom)
Pressure (GPa)

Fig. 1

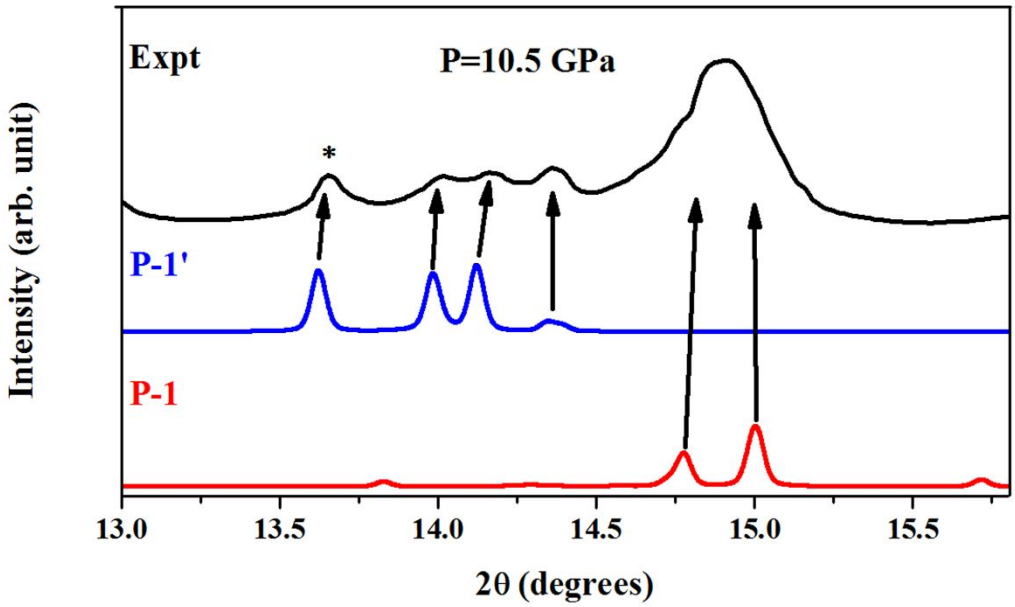
Expt
P=10.5 GPa
*
P-1'
P-1
Intensity (arb. unit)
13.0
13.5
14.0
14.5
15.0
15.5
2θ (degrees)

Fig. 2

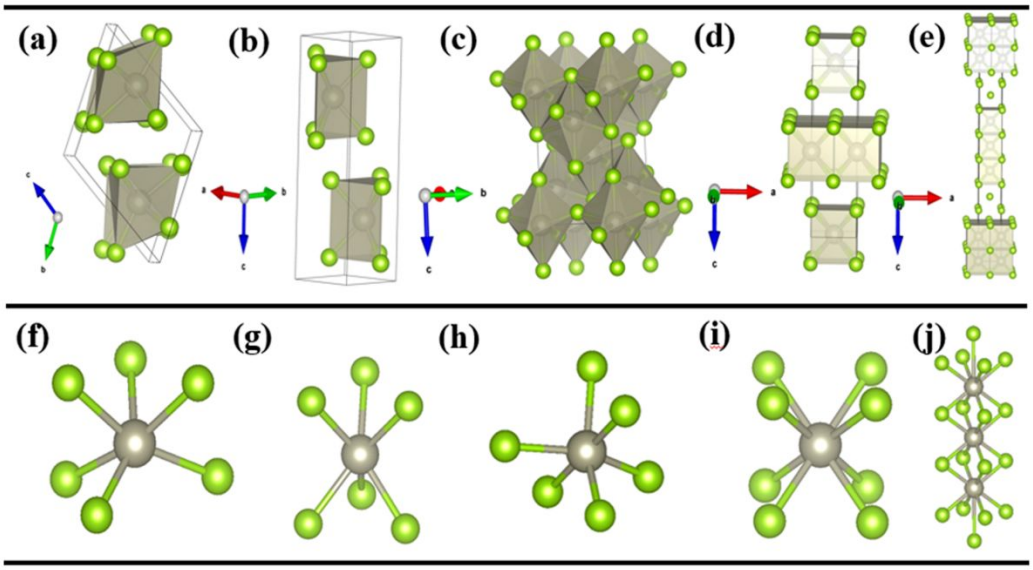

Fig. 3

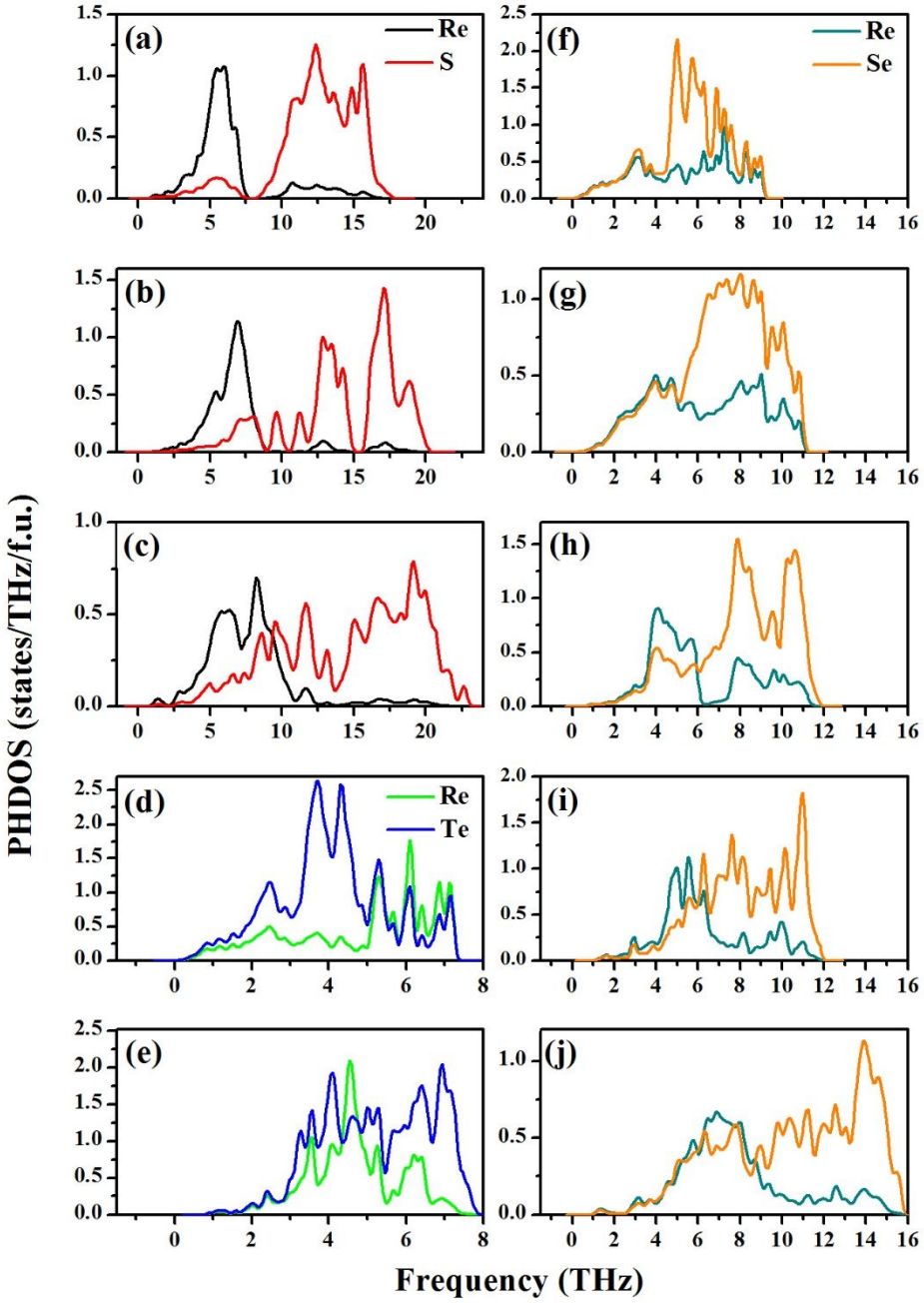

Fig. 4

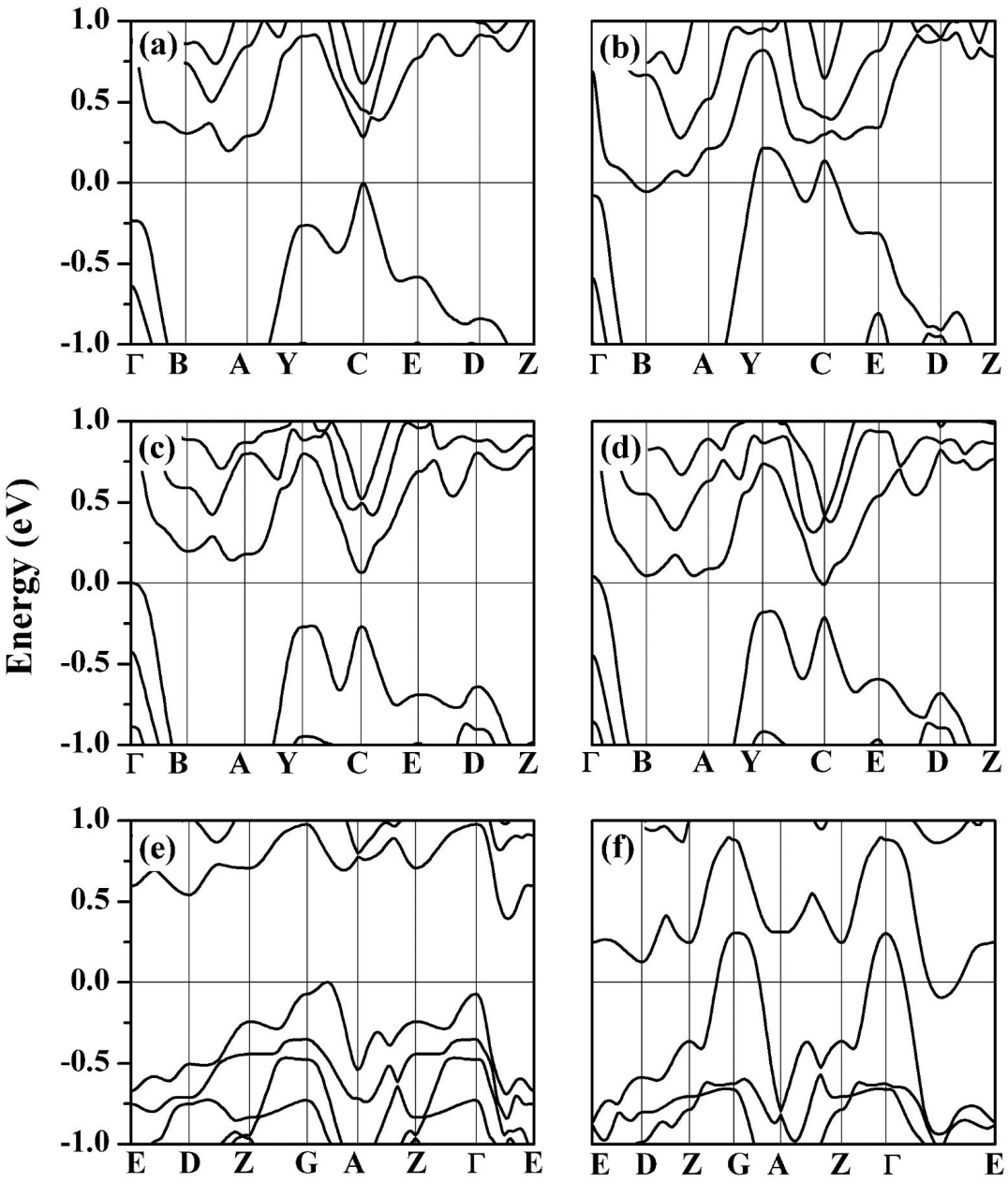

Fig. 5

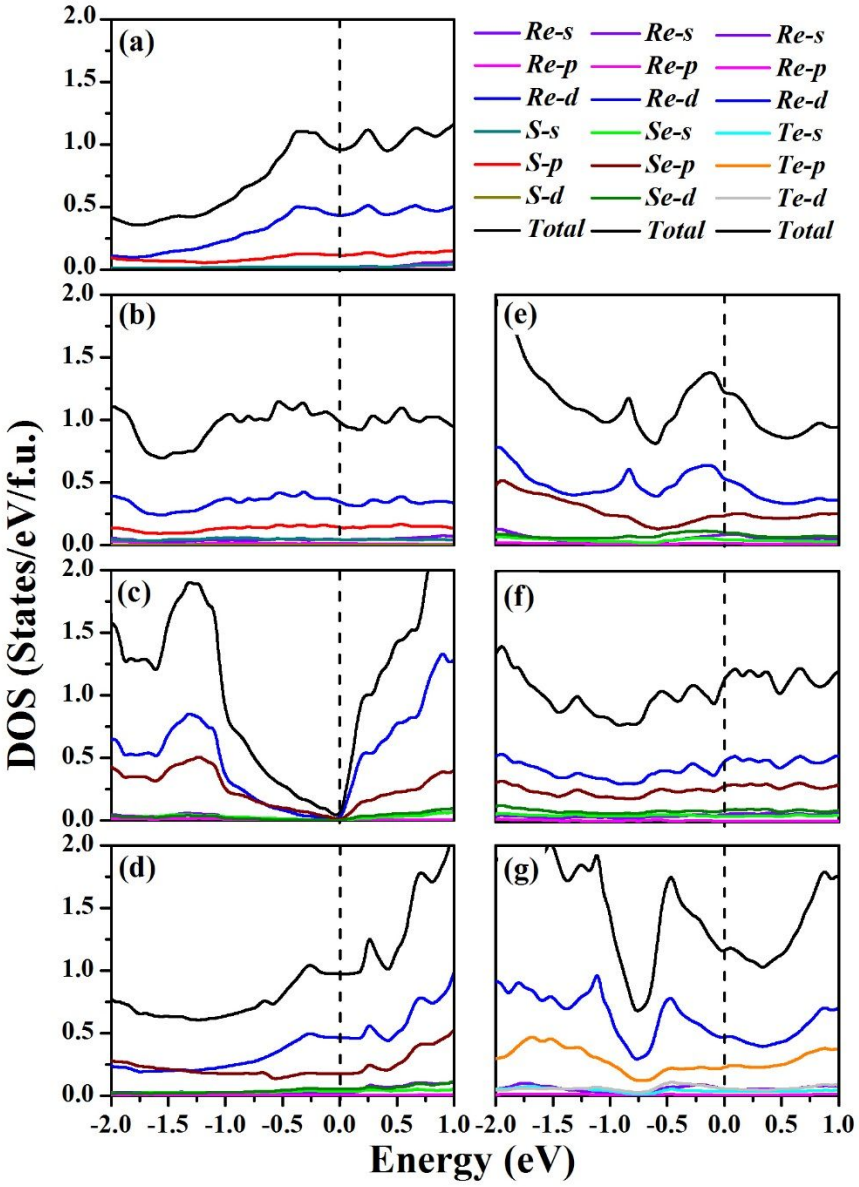
(a)
(b)
(c)
(d)
(e)
(f)
(g)
Re-s
Re-p
Re-d
S-s
S-p
S-d
Se-s
Se-p
Se-d
Te-s
Te-p
Te-d
Total
DOS (States/eV/f.u.)
Energy (eV)

Fig. 6

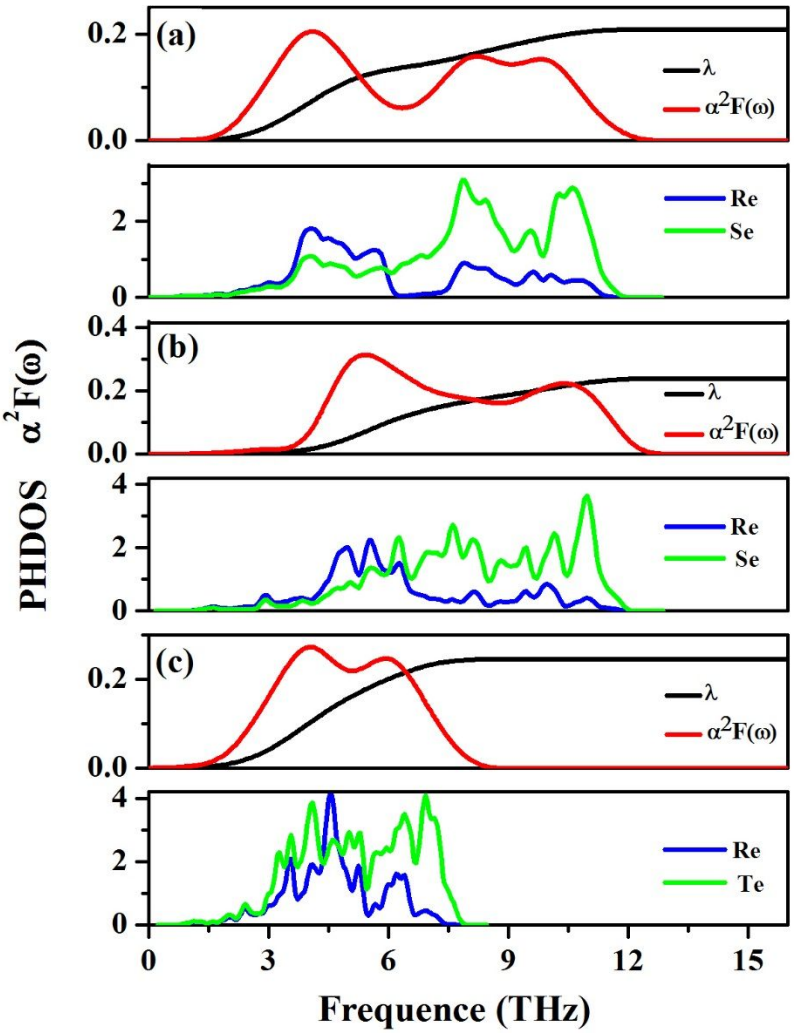
(a)
(b)
(c)
λ
α²F(ω)
Re
Se
Te
PHDOS α²F(ω)
Frequence (THz)
0.0
0.2
0.4
0
2
4
0
3
6
9
12
15

Fig. 7

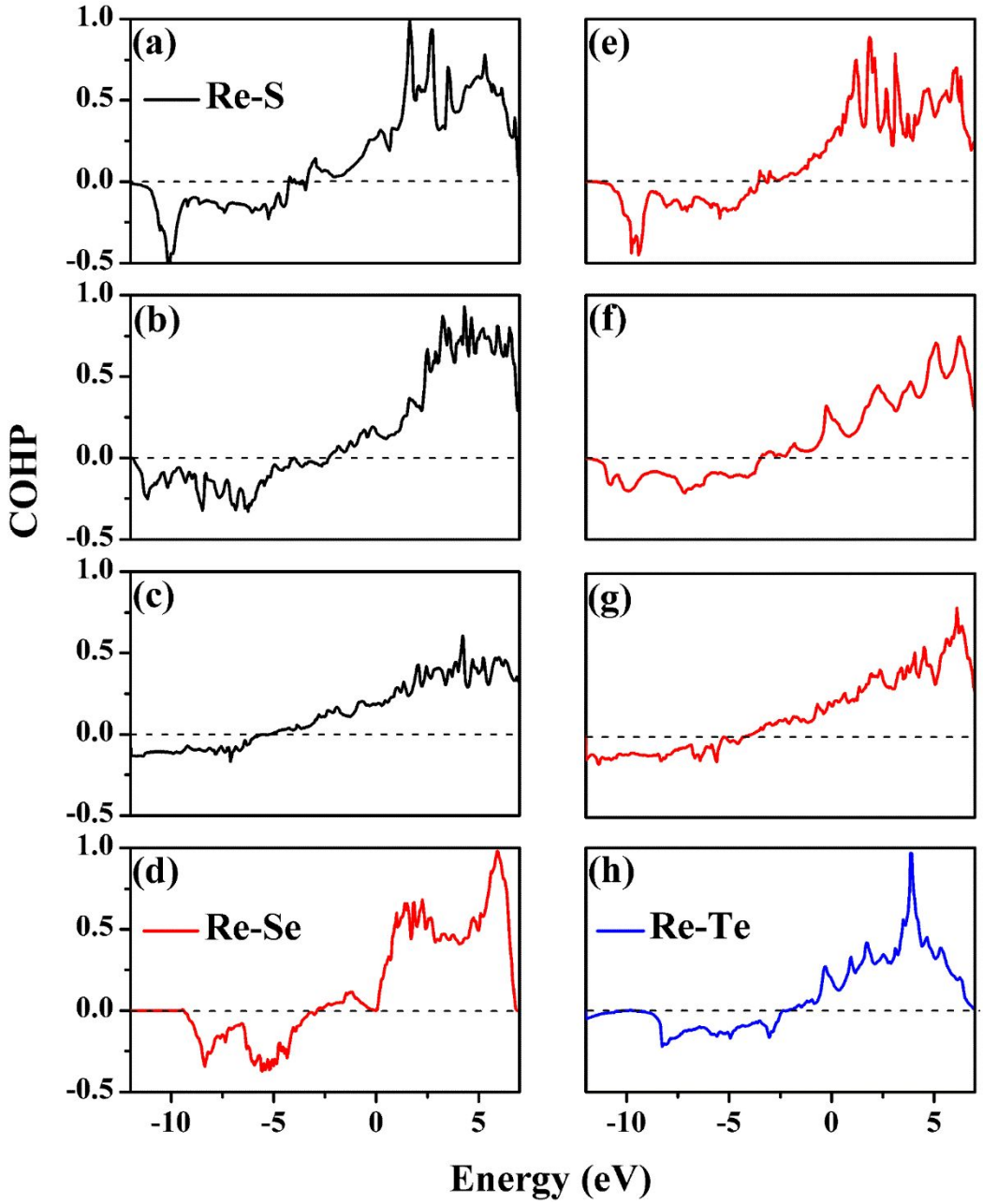

Fig. 8

Table Caption:

Table 1 Comparison of the calculated lattice parameters and volumes at 0 GPa using the GGA-PBE functional and optB86b functional with vdW-DF correction with experimental values.

Table 2 The ICOHP value of new predicted phases of ReS_2 $ReSe_2$ and $ReTe_2$.

Table 3 Structural information of new phases of ReS_2 $ReSe_2$ and $ReTe_2$.

	ReS_2 (*P*-1)			$ReSe_2$ (*P*-1)			$ReTe_2$ (*P*-1)		
	PBE	**optB86b**	**expt**	**PBE**	**optB86b**	**expt**	**PBE**	**optB86b**	**expt**
a (Å)	**6.396**	**6.364**	**6.352**	**6.648**	**6.616**	**6.597**	**7.259**	**7.219**	**7.180**
b (Å)	**6.501**	**6.466**	**6.446**	**6.770**	**6.738**	**6.710**	**7.073**	**7.048**	**6.548**
c (Å)	**13.489**	**12.724**	**12.779**	**7.197**	**6.728**	**6.721**	**7.839**	**7.369**	**7.512**

Table 1

ICOHP PHASE	ReS_2 (Re-S)	$ReSe_2$ (Re-Se)
P-1′	---	-3.54 (40 GPa)
$P6_3/mmc$	-3.48 (97 GPa)	-3.33 (100 GPa)
$I4_1/amd$	-3.74 (100 GPa)	---
I4/mmm	---	-2.97 (150 GPa)
I4/mmm′	-2.70 (300 GPa) -2.78 (300 GPa)	-1.34 (240 GPa) -2.81 (240 GPa)

Table 2

systems	Pressure	Space group	Lattice Parameter (Å, °)	Atom	Atomic coordinates (fractional)		
					x	y	z
ReS_2	97 GPa	$P6_3/mmc$	a=b=2.734,c=10.128	Re(2d)	0.667	0.333	0.250
			α=β=90, γ=120	S(4f)	0.667	0.333	0.913
	140GPa	$I4_1/amd$	a=b=4.230,c=6.698	Re(4a)	1	-0.5	0.75
				S(8e)	0.5	0	0.587
	300 GPa	$I4/mmm'$	a=b=2.560,c=22.376	Re(4e)	0	0	0.5
			α=β=γ=90	Re(4e)	0.5	0.5	0.116
				S (4e)	0.5	0.5	0.325
				S(4e)	0.5	0.5	0.442
				S (4e)	0	0	0.277
$ReSe_2$	40 GPa	P-1′	a=6.341, b=6.081, c=6.066	Se(2i)	0.182	0.746	0.57
			α=116.340, β=75.508, γ=75.219	Se(2i)	0.370	0.218	0.359
				Se(2i)	0.693	0.280	0.013
				Se(2i)	0.142	0.301	0.066
				Re(2i)	0.487	0.220	0.708
				Re(2i)	0.933	0.806	0.331
	80 GPa	$P6_3/mmc$	a=b=2.832, c=11.286	Re(2d)	0.667	0.333	0.25
			α=β=90, γ=120	Se(4f)	0.667	0.333	0.907
	120 GPa	$I4/mmm$	a=b=2.707,c=9.7406	Re(2b)	0	0	0.5
			α=β=γ=90	Se(4e)	0.5	0.5	0.845
	240 GPa	$I4/mmm'$	a=b=2.681,c=25.324	Re(2a)	0	0	0
			α=β=γ=90	Re(4e)	0	0	0.109
				Se(4e)	0.5	0.5	0.173
				Se(4e)	0.5	0.5	0.196
				Se(4e)	0	0	0.663

$ReTe_2$	**60 GPa**	***I*4/*mmm***	**a=b=2.976,c=11.000**	**Re(2b)**	**0**	**0**	**0.50**
			α=β=γ=90	**Te(4e)**	**0.5**	**0.5**	**0.352**

Table 3

Table of Contents

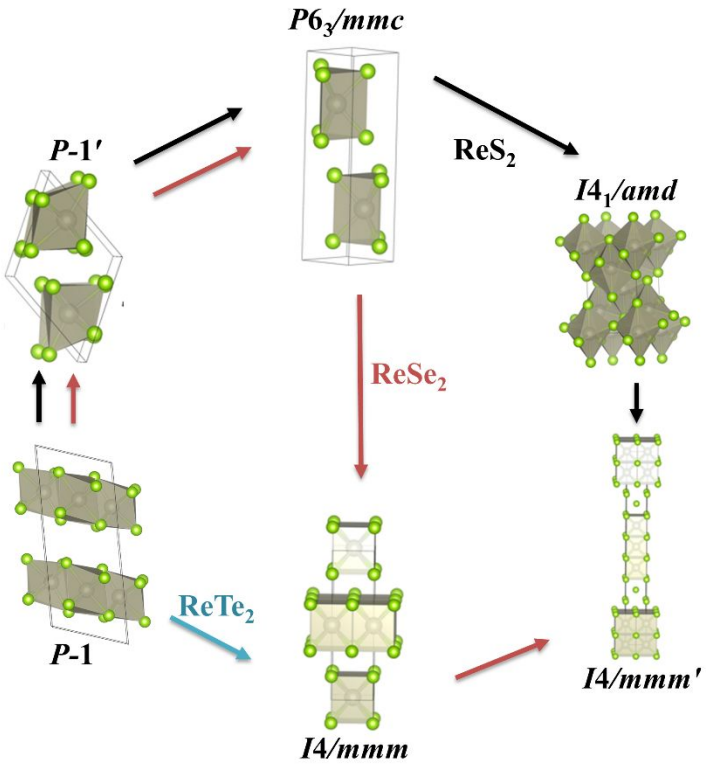

Synopsis: Five energetically stable phases of *P*-1′, *P*6$_3$/*mmc*, *I*4$_1$/*amd*, *I*4/*mmm* and *I*4/*mmm*′ were predicted in for ReX_2 compounds at high pressures. The coordination environment of Re atom changes from ReX_6 octahedra or trigonal prisms to ReX_8 cuboid coordination with increasing pressure. The high-pressure metallic phases of ReX_2 show superconductivity.